INTERNATIONAL JOURNAL FOR NUMERICAL METHODS IN FLUIDS, VOL. 19, 237–257 (1994)

DISPERSION UNDER NEUTRAL ATMOSPHERIC CONDITIONS

J. P. GLEKAS AND G. C. BERGELES

Laboratory of Aerodynamics, National Technical University of Athens, 9 Heroon Polytechniou Ave., 157 73 Zografou, Athens, Greece

SUMMARY

A recently developed mesoscale numerical model has been applied to the Athens Basin in order to provide a detailed description of the mean flow and pollution levels under neutral atmospheric conditions. The model is based on the numerical solution of the time-averaged Navier–Stokes equations written in their contravariant strong conservation form in a generalized non-orthogonal co-ordinate system. Before its application to the Athens Basin case, the reliability of the model was tested by predicting the flow and concentration fields over a three-dimensional hill. The predicted results agree favourably with available experimental data, demonstrating the validity, flexibility and economy of the model for flows in three-dimensional complex terrain.

KEY WORDS Dispersion Atmospheric flows Complex terrain

1. INTRODUCTION

The meteorological data required for the evaluation of pollutant dispersion, for wind energy applications and for the study of mesoscale circulations over complex terrain are usually available from synoptic scale networks of meteorological stations, which, however, lack sufficient resolution for detailed mapping of the wind field. In order to overcome this problem, either a dense network of monitoring stations or a mesoscale numerical model is required. Owing to the considerable expense involved and the difficulty in maintaining a dense network of surface stations for a very long time, few studies have been performed adopting the first approach.[1,2]

The second approach applies three-dimensional numerical models which solve various sets of conservation equations.[3] The major advantage in using numerical models is their capability to provide useful information for meteorological and air pollution scenarios in a fast, reliable and inexpensive way compared with the observational approach. The various kinds of numerical models correspond to the differences which are encountered in the level of assumptions regarding the flow equations or the physical domain.

A basic category of mesoscale numerical models are the linear models developed by Jackson and Hunt[4] in two dimensions and by Mason and Sykes[5] in three dimensions. These models apply an analytical perturbation theory in the surface layer flow; their linear approximations restrict their use to low hills without flow reversal.

The increase in computer power in recent years has enabled the development of numerical models which solve the full non-linear equations of motion; examples include those of Pielke,[6]

CCC 0271–2091/94/150237–22

Received March 1991
Revised February 1994

Tapp and White,[7] Anthes and Warner,[8] Pandolfo and Jacobs,[9] Schuman and Volkert[10] and more recently Glekas.[11]

This paper presents a finite volume method for the solution of the incompressible three-dimensional Reynolds equations in a non-orthogonal surface-oriented co-ordinate system. The applications presented here concern the solution of the coupled momentum equations and the transport equation of species.

The basic features which characterize the present model are as follows.

1. A three-dimensional co-ordinate transformation is used instead of the 1D vertical transformation which is used in almost all other models. Under this transformation the complex physical domain is transformed to a unit cube where the governing equations are solved. The advantages of the 3D transformation compared with the 1D vertical one are that the grid spacing in the computational space is uniform (reducing the mathematical operations per iteration) while in the physical space the grid is non-uniform depending on the ground geometry (fine near obstructions, coarse in flat areas, etc.).
2. The numerical discretization of the equations is accomplished using the finite volume technique instead of the finite difference methods based on the Taylor expansion which are usually adopted in mesoscale models.
3. Three-dimensional turbulent recirculating flows can be calculated owing to the 3D elliptic solution procedure which is used for the calculation of the pressure field.
4. The time evolution of passive contaminant releases can be calculated as well as the steady state pattern for stratified or neutral atmospheric conditions.

In subsequent sections the basic numerical approach is described; the mathematical formulation, the boundary conditions, the solution procedure and the turbulence closure are presented. For model validation its application to the calculation of the flow and concentration fields over a three-dimensional hill is described in Section 6, while in Section 7 the model is applied to predict the wind field and pollution levels due to selected pollution sources in the complex terrain of the Athens Basin.

2. MATHEMATICAL FORMULATION AND BOUNDARY CONDITIONS

In the present paper the equations are formulated in their contravariant form, with the vectors and tensors being expressed in a Cartesian basis.[11]

The transport equations for mass, momentum and species can be cast into the convenient form

$$\frac{\partial}{\partial t}(J\Phi) + \frac{\partial}{\partial X^j}(\rho V^j \Phi) = \frac{\partial}{\partial X^j}\left(J\Gamma_\Phi \alpha^j \frac{\partial \Phi}{\partial X^j}\right) + S_\Phi \quad (j = 1, 2, 3), \tag{1}$$

where ρ, V^j, Γ_Φ and S_Φ are the density, the contravariant components of the velocity vector, the exchange coefficient and the source term per unit volume respectively for the variable Φ and α^j are parameters which depend on the co-ordinate transformation. The source and exchange coefficients for velocities and scalar quantities and the parameters α^j have been discussed elsewhere[11,12] and the details are not repeated here. However, details of the closure models which are adopted in this work are discussed in the following section.

The physical domain is transformed into a unit cube (Figure 1) where the equations are solved. The solution domain is oriented so that the inlet plane 1 lies normal to the approaching wind. The flow through this surface is assumed to be a boundary layer type of flow corresponding to

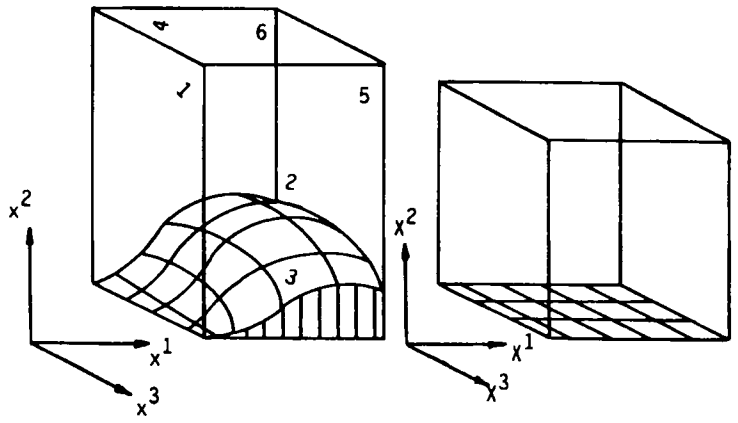

Figure 1. Physical and solution domains

the experimental data. The lateral surfaces (5 and 6) are prescribed as permeable with zero tangential stress. The boundary conditions on the outflow surface 2 are

$$u^2 = 0, \qquad \partial u^3/\partial x^1 = 0, \qquad \partial u^1/\partial x^1 = 0.$$

A Dirichlet boundary condition ($u^1 = U_\infty$) is used on the upper boundary 4, while on surface 3, the ground, a no-slip condition is imposed ($u^1 = u^2 = u^3 = 0$).

3. TURBULENCE CLOSURE

Although the fundamental momentum, energy, mass and species conservation equations are applicable to the full range of atmospheric scales, direct application in calculating atmospheric flows requires high space resolution which is beyond the available computer power. However, it is possible to approximate these processes by using a turbulence closure scheme. In this paper the eddy viscosity concept is used and the turbulent viscosity μ_t is calculated using either the modified formula suggested by Cebeci[13] (for the case of turbulent flow around the three-dimensional hill) or the mixing length formula suggested by O'Brien[14] (for the Athens Basin application). These models were chosen owing to their relative simplicity and their accurate behaviour in problems concerning the parametrization of the atmospheric boundary layer.

Cebeci's model is based on the Van Driest hypothesis, i.e. the turbulent viscosity μ_t is given by the formula

$$\mu_t = \rho l_m^2 \, \partial u/\partial y, \tag{2}$$

where l_m is the mixing length and y is the distance from the wall. Moreover, the boundary layer is split into two regions, the inner one $0 < y < y_c$ and the outer one $y_c < y < \delta$, where δ is the boundary layer height. For the respective regions the turbulent viscosity is calculated by the formulae

$$\mu_t = \rho L^2[(\partial u^1/\partial y)^2 + (\partial u^3/\partial y)^2]^{1/2}, \quad 0 < y < y_c, \tag{3a}$$

$$\mu_t = \rho a \left| \int_0^\infty \{u_\infty[(u^1)^2 + (u^3)^2]^{1/2}\} \, dy \right|, \quad y_c < y < \delta, \tag{3b}$$

where u^1 and u^3 are the parallel-to-the-wall velocity components, $L = 0.4y[1 - \exp(-y/A)]$, with $A = 26(\nu/N)/u_*$, $u_* = (\tau_s/\rho)^{1/2}$, ν the kinematic fluid viscosity, u_* the friction velocity, τ_s the wall shear stress, $N = (1 - 11{\cdot}8p^+)^{1/2}$ and $p^+ = (\mu\tau_s/\rho^{1/2})\text{grad}p$, $a = 0{\cdot}0168$ and y_c is the distance from the ground at which the values of μ_t given by relations (3a) and 3(b) become equal.

The O'Brien model is based on the similarity theory for the surface boundary layer:

$$\mu_t = ku_*y, \quad 0 < y < y_c, \tag{4a}$$

$$\mu_t = \mu_\delta + \left(\frac{y-\delta}{\delta - y_c}\right)^2 \left\{\mu_c - \mu_\delta + (y - y_c)\left[\left(\frac{\partial\mu}{\partial y}\right)_c + \frac{2(\mu_c - \mu_\delta)}{\delta - y_c}\right]\right\}, \quad y_c < y < \delta, \tag{4b}$$

where y_c and δ are the heights of the surface layer and the boundary layer respectively and μ_c and μ_δ are the turbulent viscosities at the respective locations y_c and δ.

4. NUMERICAL PROCEDURE

The numerical procedure used to solve the generalized form of the governing conservation equations (1) is described in detail in References 11 and 15. A uniform Cartesian grid is employed in the transformed space and finite difference approximations to the conservation laws are obtained by integrating equations (1) over the control volumes and discretizing them in Cartesian co-ordinates (Figure 2). A staggered mesh arrangement for the velocities is adopted and the hybrid difference scheme[16] is used to discretize the convection terms. Then the set of governing equations can be cast into the general form

$$A_P\Phi_P = A_E\Phi_E + A_W\Phi_W + A_N\Phi_N + A_S\Phi_S + A_U\Phi_U + A_D\Phi_D + S_\Phi, \tag{5}$$

where the coefficients A_i link the value Φ_P with the values of the six neighbouring i-nodes (Figure 2).

The pressure field is gradually established through pressure corrections P' in such a way as to satisfy global and local continuity. A pressure correction equation of the general form (5) is solved with $\Phi = P'$. This equation is a three-dimensional elliptic equation and is solved as such in this work.[11]

The calculation procedure starts from an initial guess for the flow and pressure fields and the non-linear algebraic equation set (5) for the momentum and pressure correction is solved iteratively until convergence is obtained, i.e. the mass imbalance becomes less than a small fraction ε of the inlet mass flow m_{inlet} ($\varepsilon = 10^{-3}m_{\text{inlet}}$).

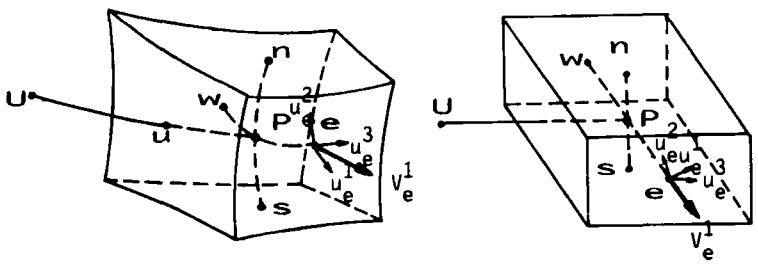

Figure 2. Control volume representation (physical and transformed spaces)

5. GENERATION OF THE CO-ORDINATE SYSTEM

The method for the generation of non-orthogonal body-fitted grids[17] which is employed in this work is based on the solution of an elliptic system of equations which utilizes the transformation $x^i = x^i(X^i)$ (Figure 1). After interchanging the dependent and independent variables, the system is written as

$$\alpha_1(r_{\xi\xi} + \varphi r_\xi) + \alpha_2(r_{\eta\eta} + \psi r_\eta) + \alpha_3(r_{\zeta\zeta} + \omega r_\zeta) + 2(\beta_1 r_{\xi\eta} + \beta_2 r_{\xi\zeta} + \beta_3 r_{\eta\zeta}) = 0, \tag{6}$$

where $r = (x^1, x^2, x^3) = (x, y, z)$, $\xi = X^1$, $\eta = X^2$, $\zeta = X^3$, $\alpha_i = g_{jj}g_{kk} - (g_{jk})^2$ and $\beta_i = g_{ik}g_{jk} - g_{ij}g_{kk}$, with $(i, j, k) = (1, 2, 3)$. The coefficients g_{ij} represent the metric coefficients of the transformation and φ, ψ and ω are forcing parameters allowing the construction of the grid lines at prespecified locations.

6. VALIDATION TESTS—FLOW AND CONCENTRATION FIELDS OVER A THREE-DIMENSIONAL HILL

The numerical model was used to calcualte the velocity and concentration fields around an axisymmetric hill under neutral flow conditions. The results were compared with measurements conducted in the wind tunnel of the U.S. Environmental Agency's Fluid Modelling Facility.[18]

The axisymmetric hill was an idealized version of the Cinder Cone Buttle hill located in Southern Idaho. The model hill is described by the relation

$$h(r) = \frac{h_0 + c}{1 + (rL^{-1})^4} - c, \tag{7}$$

where $h_0 = 155$ mm, $L = 388$ mm and $c = 10$ mm for $r < 755$ mm, and $h(r) = 0$ for $r > 755$ mm. The top of the model hill is a flat plateau about 400 mm in diameter. The maximum terrain slope is about 24°, causing, as the experiments indicate, flow separation on the lee side of the hill. The flow is turbulent with a Reynolds number based on the hill height equal to 35,400.

The results presented here have been obtained using two different numerical grids of $35 \times 29 \times 25$ and $53 \times 39 \times 49$ points in the directions x^1, x^2 and x^3 respectively.

Figures 3(a) and 3(b) show the geometrical configuration of the application and the three-dimensional grid around the hill respectively. The boundary conditions are those described in Section 2. On the inlet plane the velocity profile was taken from the available experimental data.[18] The grid nodes were gathered near the ground; more than half of the 29 grid nodes in the vertical direction were placed inside the thickness of the separating boundary layer. The iterative solution procedure was regarded as converged when the sum of the non-dimensionalized flux imbalance was less than 10^{-3} for the momentum and 10^{-5} for the species.

In Figure 4 the predicted mean velocity field over the hill is plotted. The numerical predictions indicate a recirculation zone on the downwind side of the hill, which is confirmed by the experimental data.[18] Although a relatively simple zero-equation turbulence model was used, the size of the recirculation zone was predicted quite accurately. According to the present numerical predictions, the separation zone begins at a distance of $2h_0$ (where h_0 is the maximum hill height) downwind of the hill top and extends for a streamwise distance of about $1.82h_0$, while the experiments show a separation region of length $1.95h_0$ starting at a point $1.73h_0$ downwind of the hill top (difference less than 7%).

Figure 5 shows the vertical velocity distributions at three locations, namely, upwind, at the top and downwind of the hill. The velocities are presented scaled by the freestream velocity U_0.

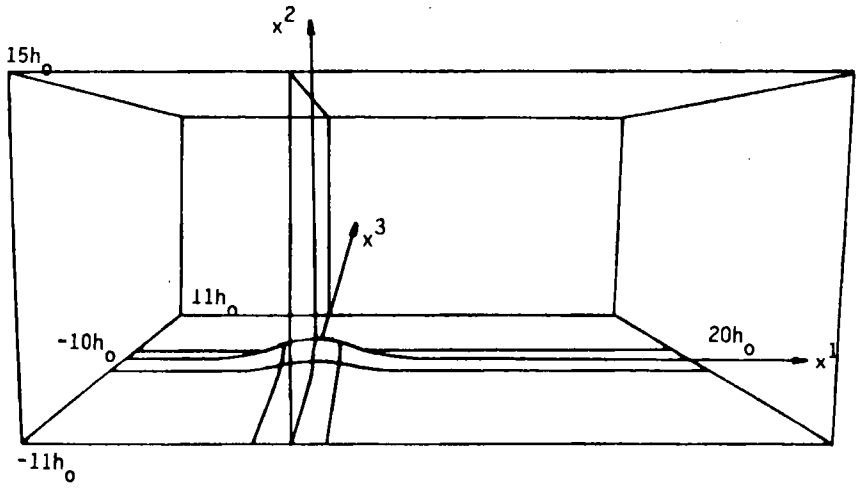

Figure 3(a). Geometrical configuration of the hill

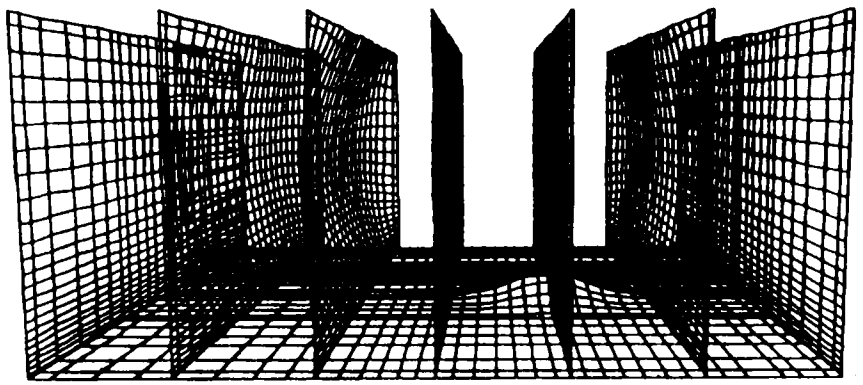

Figure 3(b). Three-dimensional grid over the hill

Results are presented for the two different grids employed, showing little difference between them. Thus it is evident that the results are grid-independent. The predicted distributions are in good agreement with the experiments. The differences are very small at the upwind base and top of the hill, while some discrepancies are observed at the downwind base of the hill ($x^1/h_0 = 5$) which are removed when the fine grid is employed. In a recent work by Tryfonopoulos[19] on the same application as in this study, the employment of two different turbulence models (the one used in this paper and the k–ε turbulence model) revealed that the k–ε model tends to overestimate the velocities near the hill surface up to a distance of one hill height above the ground. Then the velocity distributions match very well. Thus it can be argued that the discrepancies between the numerical predictions and the experiments on the downwind side of the hill can be attributed mainly to the numerical grid used.

The concentration field created by a point source located at various positions relative to the hill top was then calculated. The exchange coefficient Γ_Φ is calculated by the relation $\Gamma_\Phi = \alpha\mu_t$,

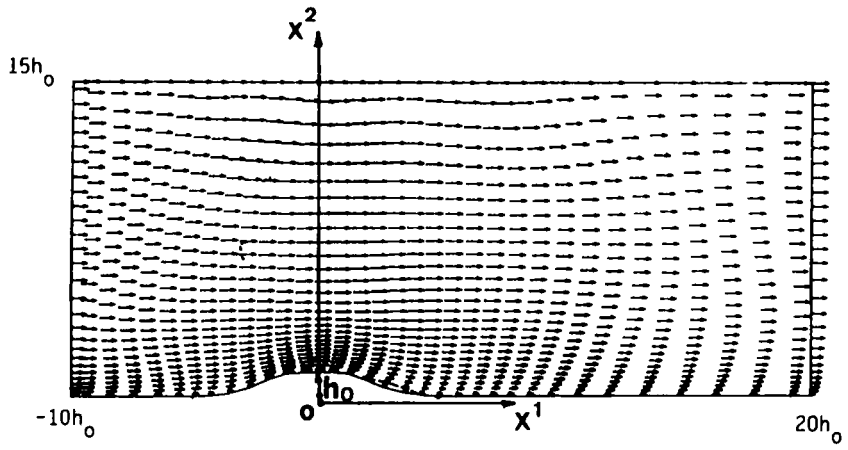

Figure 4(a). Mean velocity field at the symmetry plane of the hill ($x^3/h_0 = 0$)

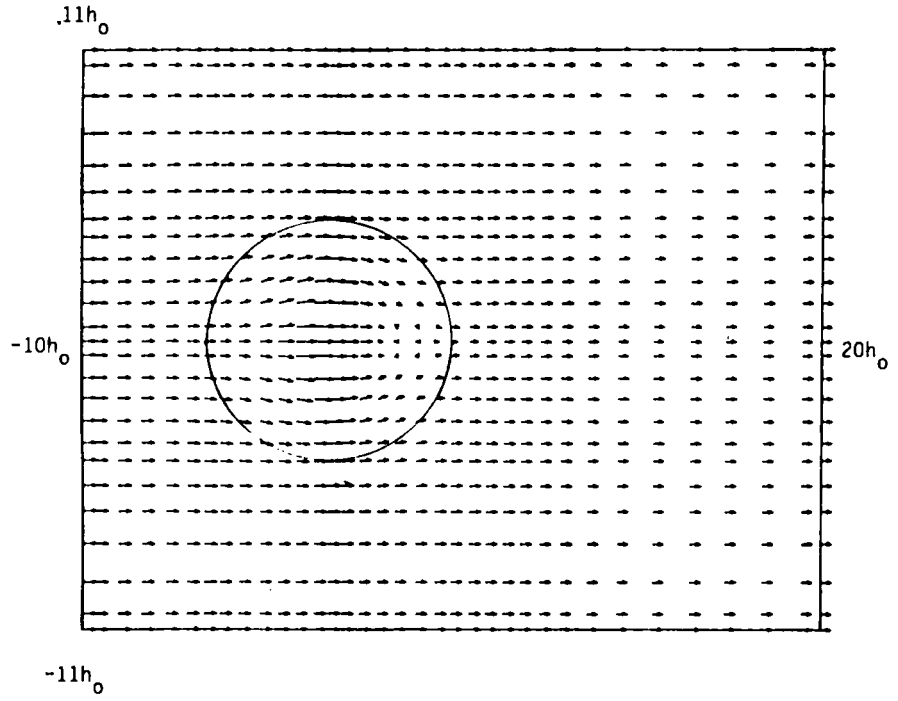

Figure 4(b). Mean velocity field (top view) at a distance $x^2/h_0 = 0.14$ from the ground

where α for neutral atmospheric conditions is given by $\alpha = 1/\sigma_c$,[20] with σ_c the species Schmidt number ($\sigma_c = 0.9$).[21]

Figure 6(a) shows the ground level concentration at the symmetry plane of the hill when the point source is located at $x^1/h_0 = 5$ upwind from the top of the hill and the stack height is $h_s = h_0$. The concentrations are normalized by the quantity Q/H^2U_0, where Q is the effluent flow rate in $cm^3\ min^{-1}$, U_0 is the freestream speed and $H = h_0$ is the height of the hill.

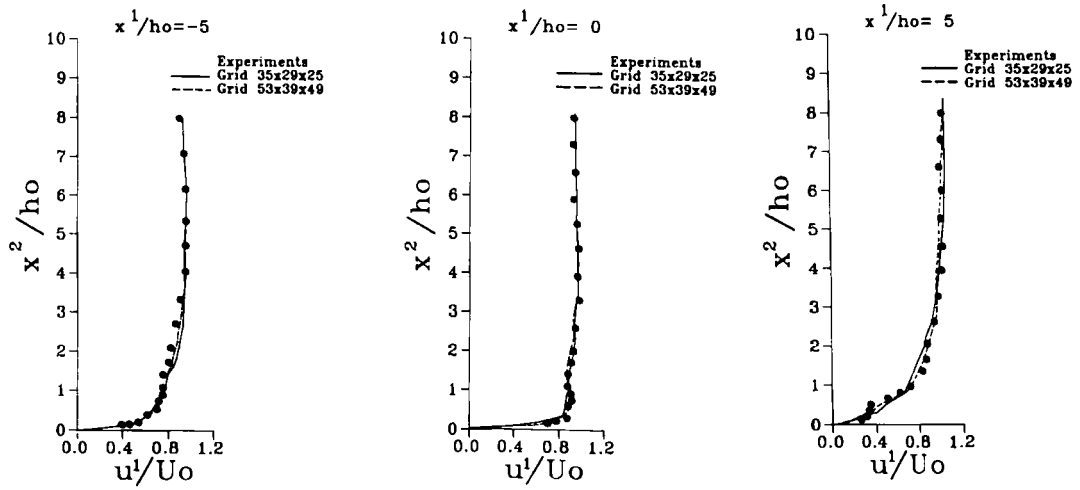

Figure 5. Vertical distributions of the u^1-component of the velocity at various locations (a) upwind, (b) at the top and (c) downwind of the hill

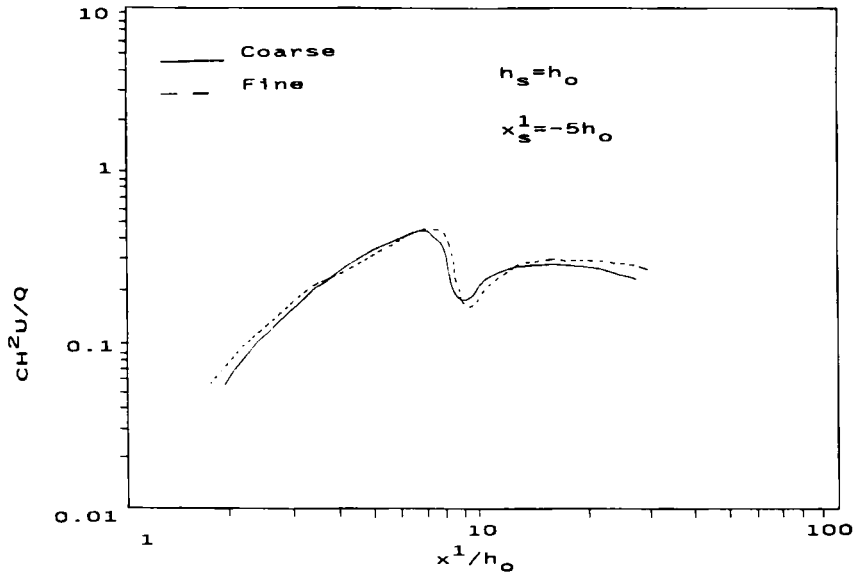

Figure 6(a). Ground level concentration at the symmetry line; $x^1/h_0 = 5$ upwind of the hill top, $h_s = h_0$, x^1 is measured from stack

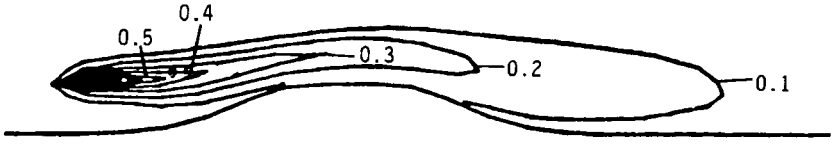

Figure 6(b). Field concentrations at the symmetry plane of the hill; $x^1/h_0 = 5$ upwind of the hill top, $h_s = h_0$, x^1 is measured from the stack

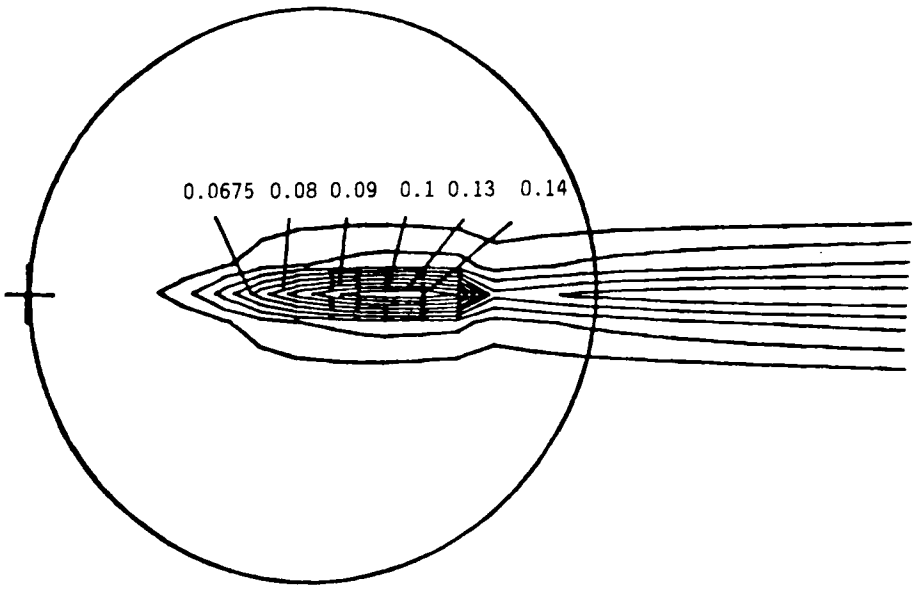

Figure 6(c). Lines of constant ground level concentration; $x^1/h_0 = 5$ upwind of the hill top, $h_s = h_0$

From this figure it is apparent that at a distance of about eight hill heights from the point source there is a sudden reduction in the ground level concentration. At this location there is a small recirculation bubble in the flow field and a small quantity of the pollutant is trapped inside it. The maximum ground level concentration occurs at a distance of $x^1/h_0 = 7$ from the point source, while the experimental value was near $x^1/h_0 = 8$.

The employment of the fine grid showed that the sudden reduction in the ground level concentration occurs at a distance of nearly nine hill heights from the point source and consequently the local maximum occurs at a distance of eight hill heights from the point source, which is in agreement with the experimental data.

In Figure 6(b) the contours of field concentration as a percentage of the concentration at the stack exit are presented. Owing to the neutral conditions which are simulated, the pollutant plume goes to the top and over the hill and the maximum concentration occurs on its lee side.

The contours of surface concentration are presented in Figure 6(c). It is of interest to note that after the stack and owing to the outward motion of the flow upwards from the top, a significant dispersion of the plume is observed. On the lee side of the hill, owing to the inward motion of the flow, the opposite phenomenon is observed.

Figure 7(a) shows comparisons between the predicted ground level concentrations and measurements at the symmetry plane of the hill when the point source is located at $x^1/h_0 = 4$ and 8.3 downwind from the top of the hill and the stack height is $h_s = 0{\cdot}77h_0$. Again the concentrations are normalized by the quantity Q/H^2U_0.

From this figure it can be seen that when the source is located at $x_s^1 = 8{\cdot}3h_0$, the maximum ground level concentration (GLC) shifts further away from the emission point compared with the case of $x_s^1 = 4h_0$. This is because the near-hill downward vertical component of the velocity vector for the latter case is larger, resulting in bending of the plume axis towards the ground.

The vertical concentration profiles at four locations downwind of the source for a source location at a distance of $x_s^1 = 4h_0$ from the hill top and at a height $h_s = h_0$, are shown in Figure

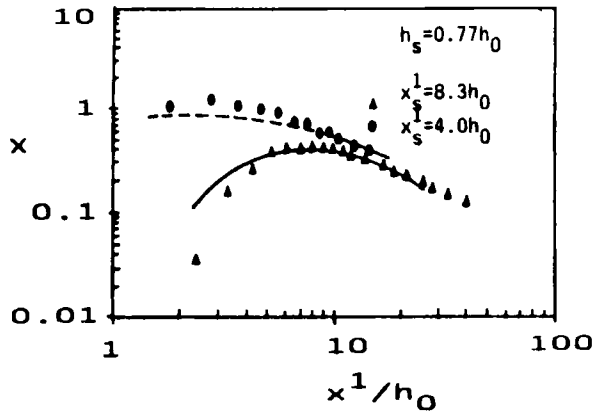

Figure 7(a). Ground level concentrations

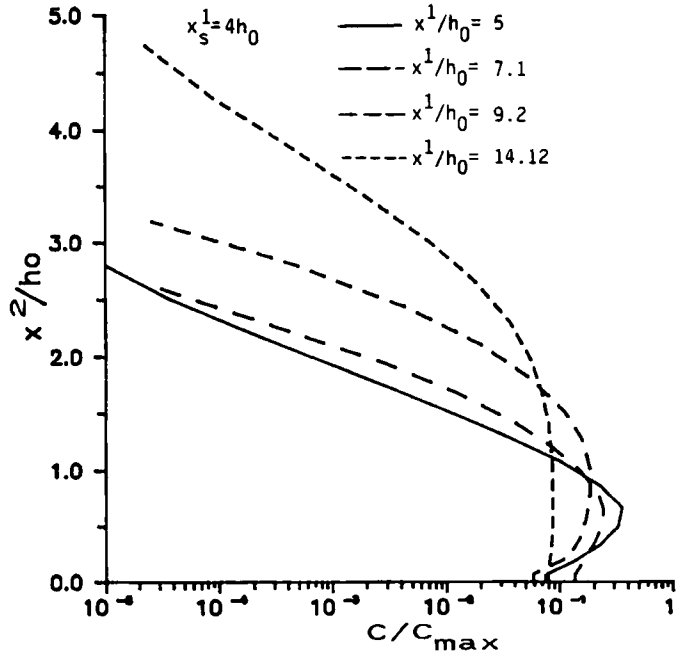

Figure 7(b). Vertical distribution of the concentration at various locations downwind of the source; $x_s^1 = 4h_0$, $h_s = 0.77h_0$

7(b). An elevated maximum seems to occur up to a distance of about $9h_0$ from the source, while far downstream, away from the region of significant downward motion, the concentration profiles decrease monotonically with height, being similar to those found in pollutant release at the ground in an undisturbed boundary layer.

In Figures 7(c) and 7(d) the contours of surface concentration as a percentage of the concentration at the stack exit are presented for the two stack locations given above. It is of interest to note that after the stack and owing to the inward motion of the flow on the lee side

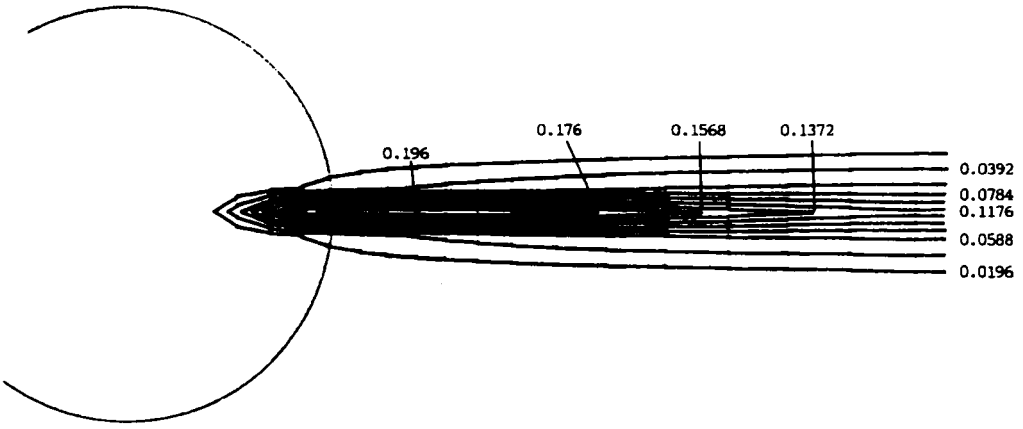

Figure 7(c). Lines of constant ground level concentration; $x_s^1 = 4h_0$, $h_s = 0{\cdot}77h_0$

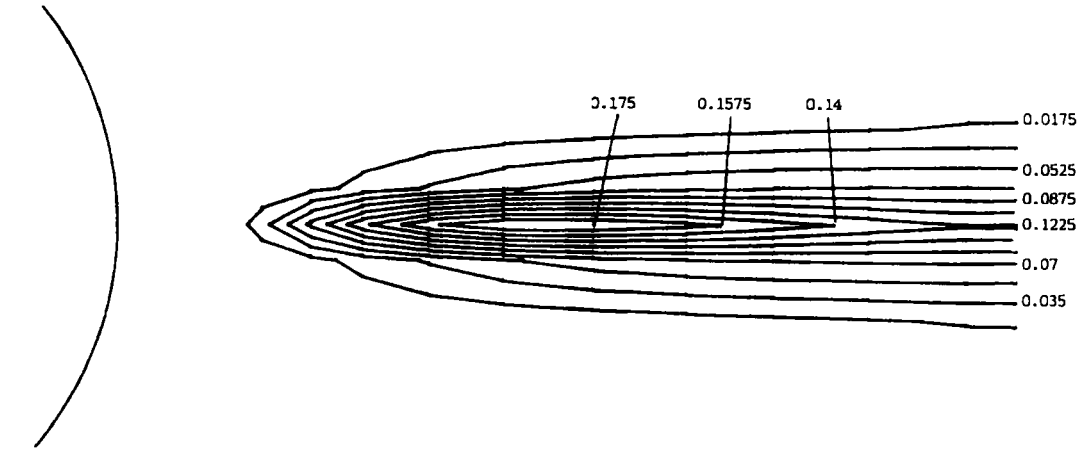

Figure 7(d). Lines of constant ground level concentration; $x_s^1 = 8{\cdot}3h_0$, $h_s = 0{\cdot}77h_0$

of the hill, there is a restriction on the pollutant dispersion in the crosswind direction. When the stack is located at $x_s^1 = 8{\cdot}3h_0$, the crosswind restriction of the pollutant dispersion is less than when the stack is located closer to the hill ($x_s = 4h_0$). This is expected owing to the less severe inward fluid motion far downwind of the hill than near it (see Figure 4(b)).

7. SIMULATION OF THE FLOW AND CONCENTRATION FIELDS OVER THE ATHENS BASIN

The numerical simulation of the neutral wind and concentration fields due to elevated point sources over the complex topography of the Athens Basin is presented here.

The Athens Basin has a highly mountainous terrain, since it is surrounded by the mountains of Parnitha, Pendeli, Hymettos and Egaleo from the NW to NE sides, while at the SW boundary is the Aegean Sea. Figure 8(a) shows a three-dimensional view of the area under consideration.

The solution domain was subdivided into finite volumes using a non-orthogonal grid which

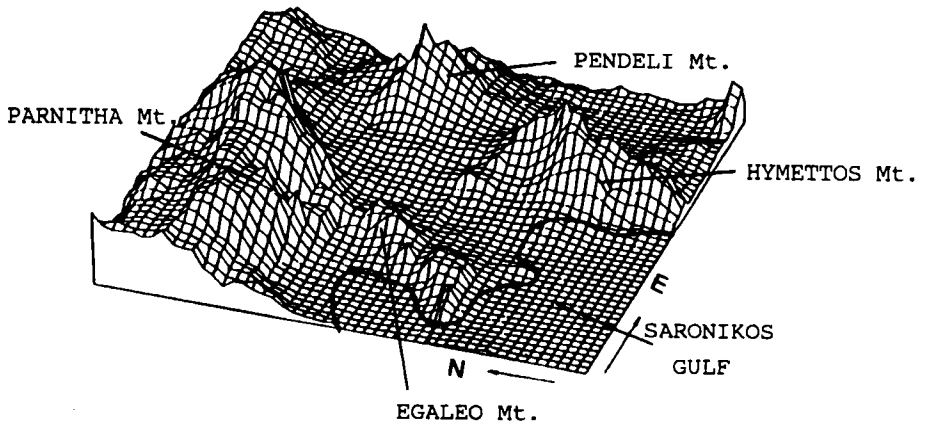

Figure 8(a). Three-dimensional view of the Athens Basin

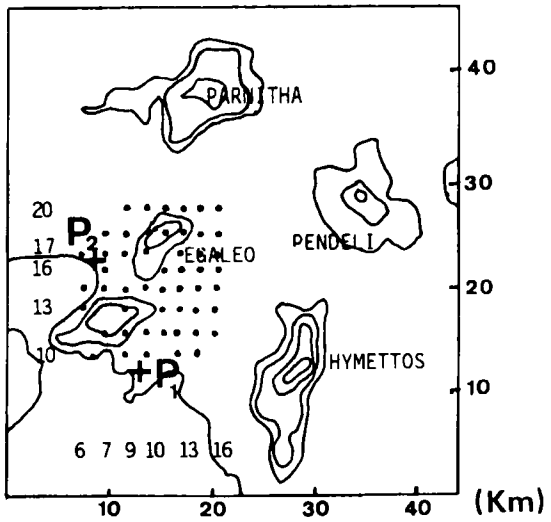

Figure 8(b). Locations where experimental data were taken

was generated using the method presented in Section 5. The elevation of the top boundary of the computational domain was set at 6000 m (i.e. nearly six times the maximum mountain height), while the horizontal dimensions of the domain were 42·5 km × 42·5 km.

The flow over the area was calculated for winds approaching from the west, a direction nearly free of surface obstructions and thus ensuring the reliable application of the boundary conditions. The numerical predictions were compared with experimental data taken in the wind tunnel of the National Technical University of Athens under neutral atmospheric conditions. In the experimental study a physical model of the Athens Basin was used with different scales in the horizontal and vertical directions.[22]

For physical model simulations of mesoscale phenomena (physical dimensions from 10 km to 100 km) in the wind tunnel the turbulent sublayer of the boundary layer is poorly

reproduced (owing to poor simulation of the ground relief) unless a distorted scale is used. The exaggeration of the topography helps in reproducing more accurately in the wind tunnel the turbulent characteristics of the real flow. Moreover, the adaptation of the distorted scale helps in simulating the anisotropic character of the stresses of the atmospheric boundary layer.

In neutral atmospheric flows the vertical diffusion coefficient is $1–10^4$ times less than the horizontal one; the distortion ratio can thus vary from 10^{-1} to 10^2. For cases where the Coriolis force and the Ekman spiral can be neglected, it has been proven that the distortion ratio can be of the order of 10^{-1}.

The inflow through the western boundary was assumed to be a boundary layer type of flow with a boundary layer thickness $\delta = 600$ m and with a surface roughness z_0, which was taken for the sea ($z_0 = 0.001$ m) and the land ($z_0 = 0.2$ m). The latter value corresponds to ground with medium or large roughness, which characterizes the west–south–west part of the Attica Peninsula.[22]

The locations where experimental data were taken are shown on the lay-out in Figure 8(b). At these locations, identified by the matrix of numbers shown in the figure, the comparison between the measurements and the numerical predictions for the wind and concentration fields will be made. Measurements of the wind velocity and turbulence quantities were taken at three heights above the ground, corresponding to 40, 80 and 120 m on the full scale.

Results were obtained with two numerical grids of $34 \times 29 \times 33$ (32,538) and $53 \times 39 \times 49$ (101,283) points in the directions x^1, x^2 and x^3 respectively, corresponding to horizontal grid spacings of 1.45 and 0.5 km respectively. In the vertical direction the grid points were clustered near the ground, with the first co-ordinate surface placed at 21 and 12 m above it respectively.

The CPU time needed per iteration and grid point was 1.1 ms on a Dec 3200 workstation, while the CPU memory required was 3.4 Mbyte for the coarse mesh and 10.5 Mbyte for the fine one.

7.1. Mean flow

Comparisons of the predicted wind field using the two different meshes with the corresponding measurements at various locations are presented in Figure 9. The predictions of the model are also compared with the predictions of a mass-consistent model (NOABL)[23] for the same wind conditions. The NOABL code is based on the solution of the continuity equation establishing a divergence-free flow field. It is used extensively in wind energy potential applications owing to its relative accuracy and very low computational cost.

Figures 9(a) and 9(b) are typical examples of the degree of agreement between predictions and measurements. At these locations the numerical predictions compare reasonably well with the experimental data (locations 9–13 and 7–16 in Figure 8(b) respectively). These locations refer either to the top of mountains (location 9–13) or to locations far from high surface obstructions (location 7–16), where local characteristics of the topography dominate over the influence of the distorted scale of the physical model employed in the wind tunnel simulation.[22,24,25]

However, at locations in the nearby region of mountains or surface obstructions the discrepancies between numerical predictions and measurements are large (Figure 9(c), corresponding to location 9–10 in Figure 8(b)). This can be attributed to the insufficient numerical resolution of the topography (compared with its representation in the physical model), to the experimental uncertainties and possibly to the distorted scale of the physical model, which is expected to have an exaggerated decelerating effect on the velocities at such sites.

The dependence of the predictions on the grid size is also shown in Figure 9. The fine mesh calculations are in better agreement with the experiments than those of the coarse mesh and the

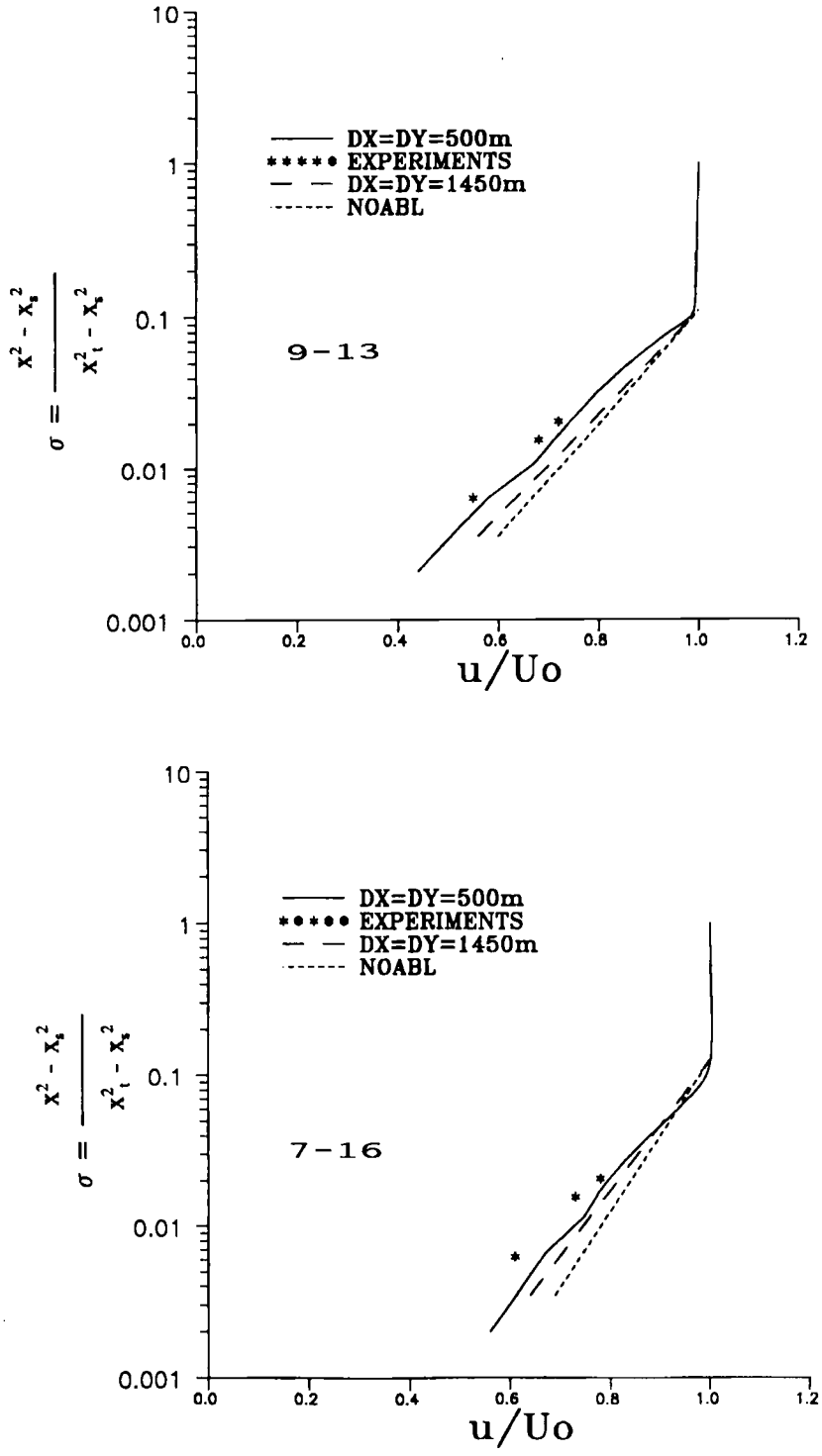

Figure 9. Vertical distributions of the u^1-component of the velocity: (a) $x^1/L = 0{\cdot}24$, $x^3/B = 0{\cdot}37$; (b) $x^1/L = 0{\cdot}337$, $x^3/B = 0{\cdot}454$; (c) $x^1/L = 0{\cdot}27$, $x^3/B = 0{\cdot}24$; x_s^2, surface elevation; x_t^2, upper boundary elevation (L and B are the length and width of the terrain)

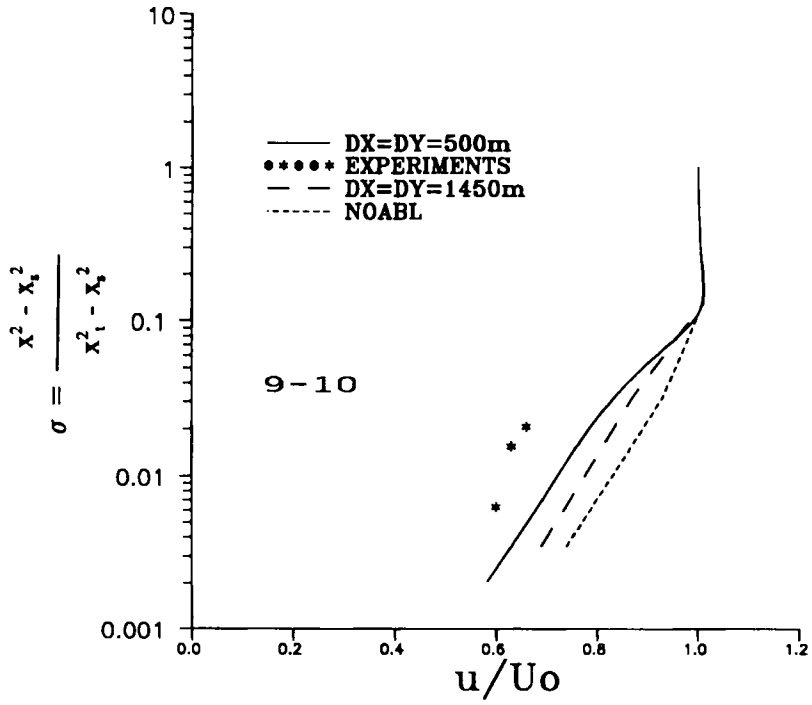

Figure 9. (*Continued*)

NOABL predictions, especially near the ground. From Figure 9(c), which corresponds to the worst agreement with the experiments, the NOABL code overpredicts the wind speed by more than 35%, compared with 20% for the coarse mesh calculations and less than 10% for the fine mesh. At the other locations the fine mesh overpredicts the wind speed by less than 5%.

The projection of the velocity vectors on to a plane for the $x^2 = 21$ m co-ordinate surface is shown in Figure 10. The dashed lines represent the surface elevation contours. A characteristic feature is the channelling of the flow between Mount Parnitha and Mount Pendeli and the deflection of the flow downwind of Mount Hymettos to the north. The wind flow over downtown Athens is diverted to the north owing to the presence of Mount Turkovunia and Mount Hymettos, which block the wind flow to the south.

7.2. Pollutant dispersion

Based on the wind field presented in the previous subsection, the transport equation for passive contaminants is solved, simulating the dispersion of pollutants emitted from two elevated point sources under neutral atmospheric conditions. The numerical predictions are compared with available experimental data obtained from measurements conducted in the wind tunnel of the National Technical University of Athens.[22] The locations of the point sources (P1 and P2) are shown in Figure 8(b). The effective heights of their stacks are $h_{\text{eff}} = 214.2$ and 135.5 m respectively.

Figure 11 shows the ground level concentration in $\mu g\,m^{-3}$ for the point source P2. The maximum GLC assuming 400 mg Nm^{-3} pollutant concentration at the stack exit is 8 $\mu g\,m^{-3}$; the corresponding experimental value was 9·7 $\mu g\,m^{-3}$. From the figure it is evident the non-symmetrical dispersion of the pollutants with respect to the plume axis is caused by the divergence of the flow field by Mount Turkovunia and Mount Hymettos, which block the wind

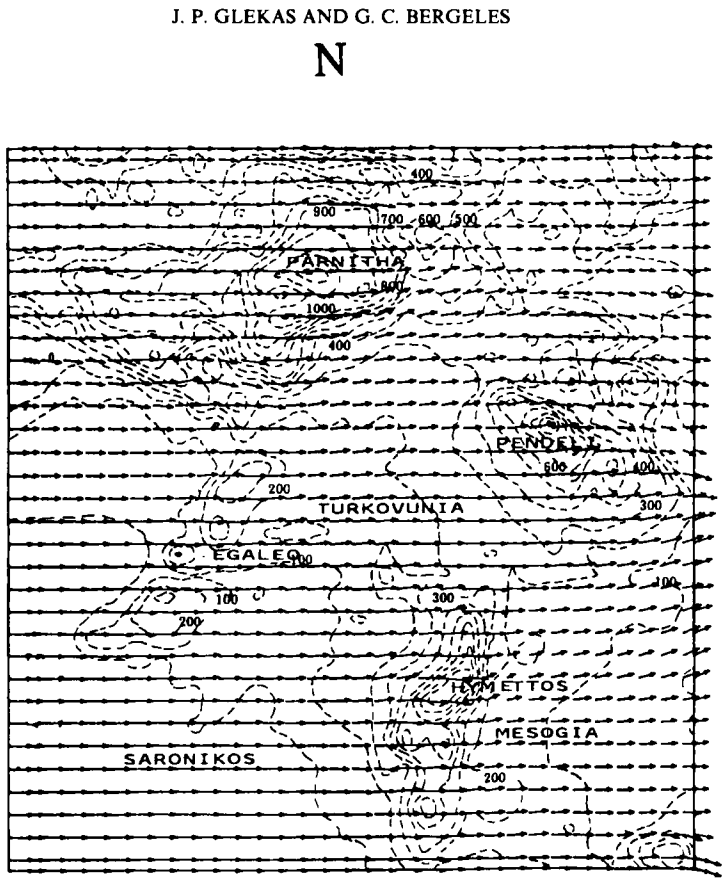

Figure 10. Mean velocity field at a distance of 21 m above the ground

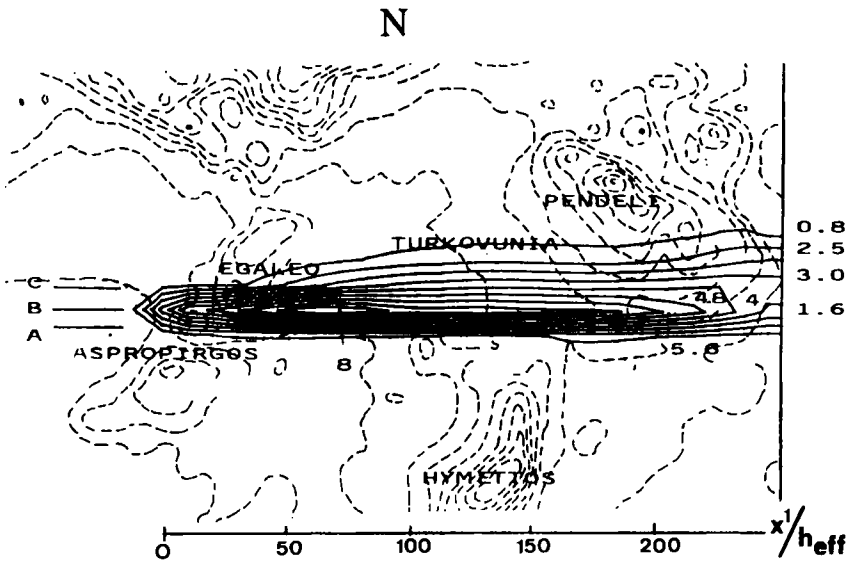

Figure 11. Contours of ground level concentration in $\mu g\ m^{-3}$

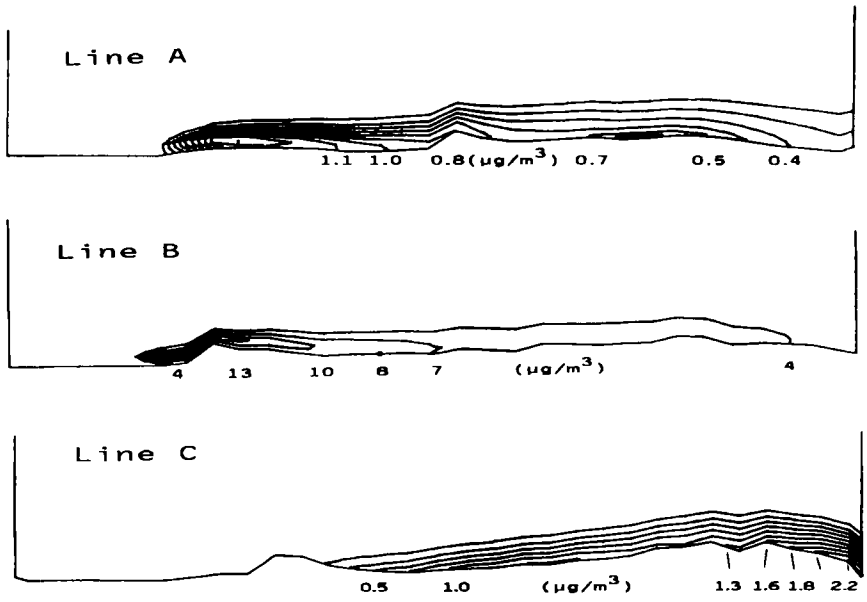

Figure 12. Contours of ground level concentration at (A) $x^3/B = 0{\cdot}424$, (B) $x^3/B = 0{\cdot}455$ and (C) $x^3/B = 0{\cdot}52$ planes

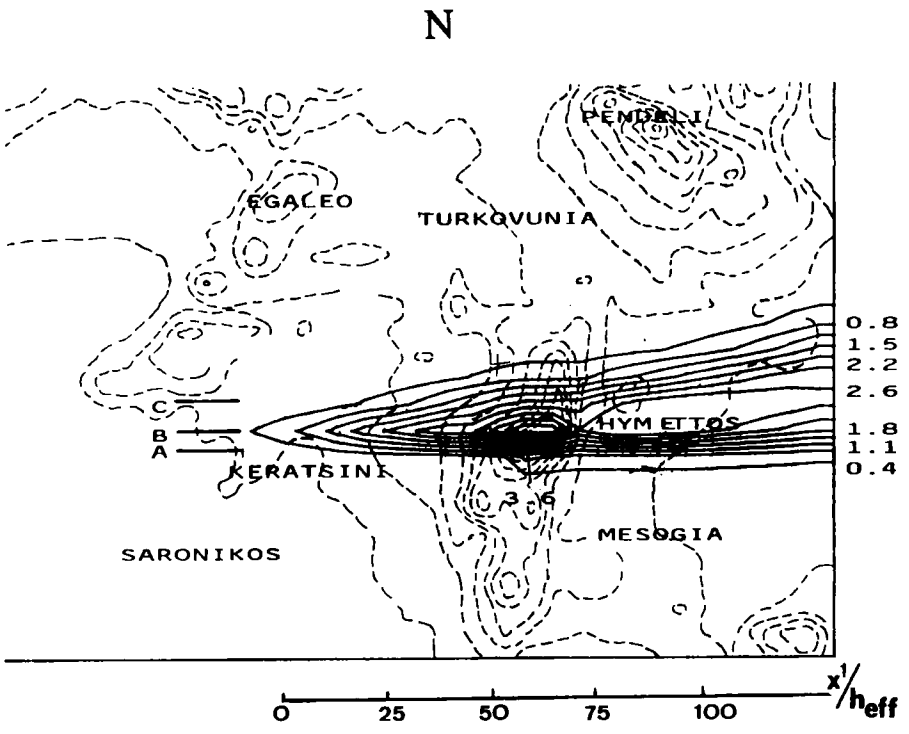

Figure 13. Contours of ground level concentration in $\mu g\ m^{-3}$

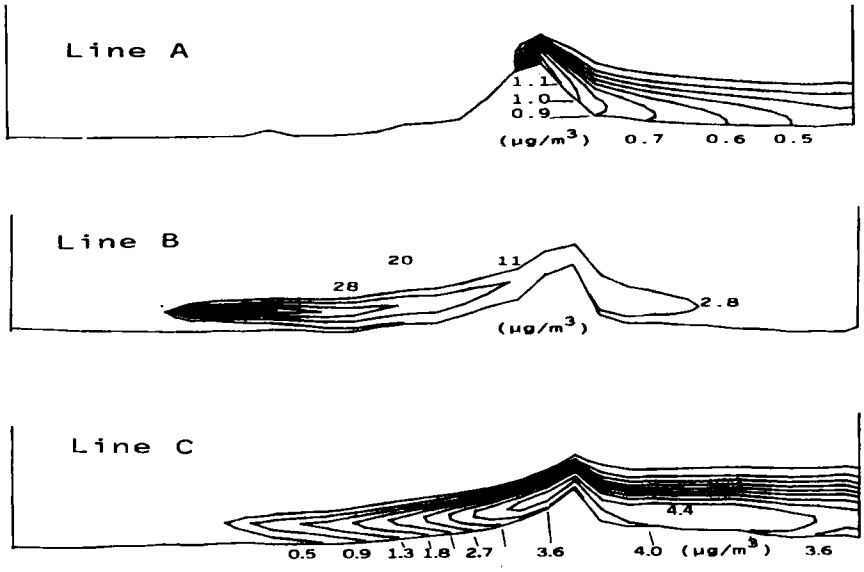

Figure 14. Contours of ground level concentration at (A) $x^3/B = 0{\cdot}239$, (B) $x^3/B = 0{\cdot}269$ and (C) $x^3/B = 0{\cdot}33$ planes

flow to the south. Moreover, it can be seen that concentrations greater than $2{\cdot}5\ \mu g\ m^{-3}$ are present in an area with normal dimension of about 5·8 km, while the corresponding experimental value was 5 km.

In Figure 12 the concentration field is presented at various longitudinal sections (corresponding to lines A, B and C in Figure 11). Owing to the high effective stack height, the pollutants travel a long distance from the source before they reach the ground. The maximum GLC in the area is located on the lee side of Mount Egaleo, while along line C the maximum GLC is located downwind of Mount Pendeli.

Figure 13 shows the surface concentration in $\mu g\ m^{-3}$ for the point source P1. The maximum GLC, again assuming a concentration level of $400\ mg\ Nm^{-3}$ at the stack exit, is $3{\cdot}6\ \mu g\ m^{-3}$; the experimental value was $2\ \mu g\ m^{-3}$. The non-symmetrical dispersion of the pollutants is stronger than in the previous case, because the plume of the pollutants is deflected sideways as it passes over Mount Hymettos.

Figure 14 shows the concentration level at various longitudinal sections.

Figure 15 shows the distributions of ground level concentration with the distance from sources P1 and P2. Predictions are also plotted using a Gaussian dispersion model for flat terrain.

Figure 15(a) corresponds to the source P2 which is located near Mount Egaleo. Owing to the immediate ground elevation downwind of the source, the present model results in considerably higher ground level concentrations than the Gaussian model, which assumes flat terrain.

In the case of point source P1 (Figure 15(b)) the source is located far upwind from Mount Hymettos and so near the source the predictions of the Gaussian model agree with the present ones. Further downwind the steep elevation of Mount Hymettos causes an elevation of the plume axis and smaller values of ground level concentrations are predicted on the upwind side of the montain compared with the concentrations obtained from the Gaussian model.

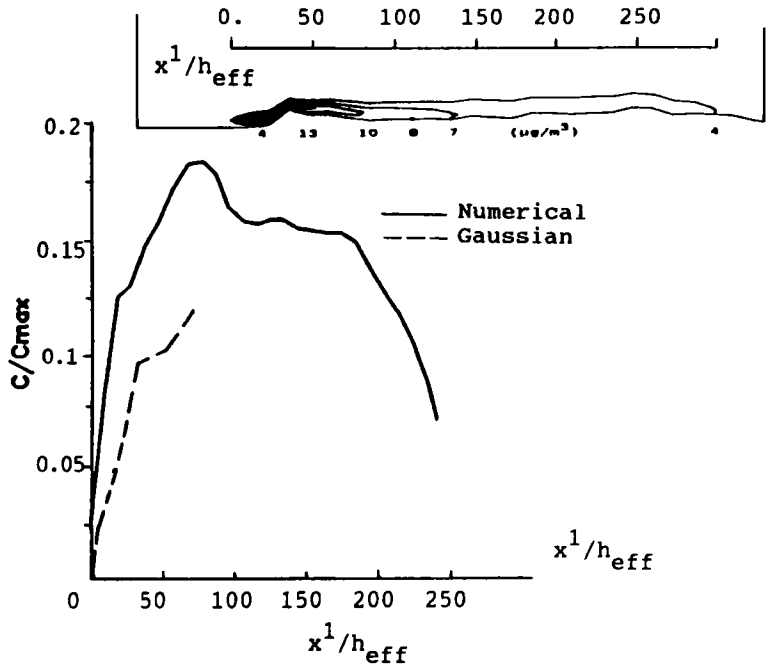

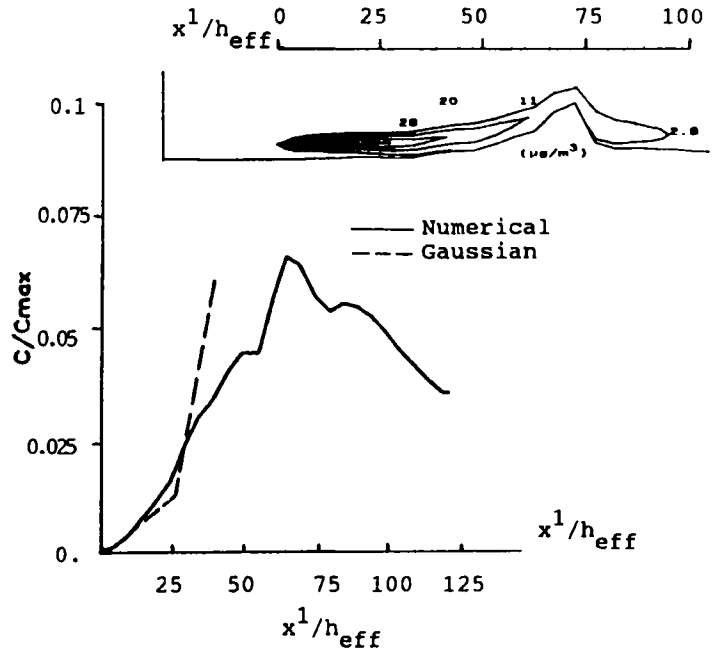

Figure 15. Distributions of the ground level concentration downwind from (a) source P2 and (b) source P1

8. CONCLUSIONS

A fully three-dimensional mathematical model for studying the air flow as well as the pollutant releases into the environment has been briefly described and its application in the complex terrain of the Athens Basin was presented. The method is based on the time-averaged Navier–Stokes equations for an incompressible fluid written in their contravariant strong conservation form in a generalized non-orthogonal system. The reliability of the model was tested by successfully predicting the flow and pollutant fields in laboratory-scaled environmental flows.

The predicted mean flow variables, flow speed-up and concentration distributions over a three-dimensional hill and over the complex terrain of the Athens Basin are in qualitative agreement with measurements, demonstrating that the model can give a sound insight to the nature of pollutant dispersion in complex terrains. The grid independence tests conducted showed an improvement in the results, especially in the Athens Basin application, giving confidence in the capabilities of the code.

As a next step the code will be extended to predict stratified flow fields and thus a complete and robust engineering tool will be available for the simulation in any detail of atmospheric dispersion of inert air pollutants.

REFERENCES

1. C. S. Keen, W. A. Lyons and J. A. Schuh, 'Air pollution transport studies in coastal zone using kinematic diagnosis analysis,' *J. Appl. Meteorol.*, **18**, 606–615 (1979).
2. B. E. Martner and J. D. Marwitz, 'Wind characteristics in Southern Wyoming,' *J. Appl. Meteorol.*, **21**, 1815–1827 (1982).
3. R. A. Pielke, 'The use of mesoscale numerical models to assess wind distribution and boundary layer structure in complex terrain', *Boundary Layer Meteorol.*, **31**, 217–231 (1985).
4. P. S. Jackson and J. C. R. Hunt, 'Turbulent wind flow over a low hill', *Q. J. R. Meteorol. Soc.*, **101**, 929–955 (1975).
5. P. J. Mason and R. I. Sykes, 'Flow over an isolated hill of moderate slope', *Q. J. R. Meteorol. Soc.*, **105**, 383–395 (1979).
6. R. A. Pielke, 'A three-dimensional numerical model of the sea breezes over South Florida', *Mon. Weather Rev.*, **102**, 115–139 (1974).
7. M. C. Trapp and P. W. White, 'A non-hydrostatic mesoscale model', *Q.J.R. Meteorol. Soc.*, **102**, 277–296 (1976).
8. R. A. Anthes and T. T. Warner, 'Development of hydrodynamic models suitable for air pollution and other mesometeorological studies', *Mon. Weather Rev.*, **106**, 1045–1078 (1978).
9. J. P. Pandolfo and C. A. Jacobs, 'Tests of an urban meteorological pollutant model using CO validation data in the Los Angeles Metropolitan Area', *1 EPA-R4-73-025a*, 1973.
10. U. Schuman and H. Volkert, 'Three-dimensional mass- and momentum consistent Helmholtz-equation in terrain following coordinates', DFVLR Institut für Physik der Atmosphere, Oberpfaffenhofen, 1984.
11. J. P. Glekas, 'Development of a method for the numerical prediction of the three-dimensional dispersion of passive contaminants. Application to the Athens Basin', *Ph.D. Thesis*, Department of Mechanical Engineering, National Technical University of Athens, 1989.
12. J. Glekas, G. Bergeles and N. Athanassiadis, 'Numerical solution of the transport equation for passive contaminants in three-dimensional complex terrains', *Int. j. numer. methods fluids*, **7**, 319–335 (1987).
13. T. Cebeci, 'Calculation of three dimensional boundary layers, I. Swept infinite cylinders and small cross flow', *AIAA J.*, **12**, 779–786 (1974).
14. J. O'Brien, 'A note on the vertical structure of the eddy exchange coefficient in the planetary boundary layer', *J. Atmos. Sci.*, **27**, 1213–1215 (1970).
15. J. P. Glekas and G. Bergeles, 'A numerical method for recirculating flows on generalized co-ordinates: application in environmental flows', *J. Appl. Math. Modell.*, **17**, 506–520 (1993).
16. S. V. Patankar, *Numerical Heat Transfer and Fluid Flow*, McGraw-Hill, New York, 1980.
17. J. P. Glekas, G. Bergeles and N. Athanassiadis, 'Numerical grid generation technique for 3D complex spaces', in G. Keramidas and C. Brebbia (eds), *Proc. 3rd Int. Conf. on Computational Methods and Experimental Measurements*, Porto Caras, 1986, pp. 905–916.
18. R. E. Lawson and W. H. Snyder, 'Estimation of pollutant concentration from sources near complex terrain in neutral flow', Meteorology and Assessment Division, Atmospheric Sciences Research Laboratory, U.S. Environmental Protection Agency, Research Triangle Park, NC, 1987.

19. D. Tryfonopoulos, 'Numerical prediction of atmospheric flows in complex terrain', *Ph.D. Thesis*, Department of Mechanical Engineering, National Technical University of Athens, 1992.
20. F. T. M. Nieuwstadt and A. P. Van Ulden, 'A numerical study of the vertical dispersion of passive contaminants from a continuous source in the atmospheric surface layer', *Atmos. Environ.*, **12**, 2119–2124 (1978).
21. B. E. Launder and D. B. Spalding, *Mathematical Models of Turbulence*, Academic, New York, 1972.
22. G. Ayeridis, 'Physical and numerical simulation of the atmospheric circulation systems over the Athens Basin', *Ph.D. Thesis*, Department of Mechanical Engineering, National Technical University of Athens, 1989.
23. R. M. Traci, G. T. Phillips and P. C. Patnaik, 'Wind energy site selection methodology development', Science Applications Inc., La Jolla, CA, 1978.
24. S. Nemoto, 'Similarity between natural local wind in the atmosphere and model wind in a wind tunnel', *Papers Meteorol. Geophys.* **19**, 131–230 (1968).
25. J. Pedlosky, *Geophysical Fluid Dynamics*, Springer, Berlin, 1982.